

Continuous-Time Analysis of AFDM: Fundamental Bounds, and Effects of Pulse-Shaping and Hardware Impairments

Michele Mirabella[‡], *Member, IEEE*, Hyeon Seok Rou[†], *Member, IEEE*, Pasquale Di Viesti[‡], *Member, IEEE*, Giuseppe Thadeu Freitas de Abreu[†], *Senior Member, IEEE*, and Giorgio M. Vitetta[‡], *Senior Member, IEEE*.

Abstract—Affine frequency division multiplexing (AFDM) has recently emerged as a resilient waveform candidate for high-mobility next-generation wireless systems. However, current literature mostly focuses on discrete time (DT) models, often overlooking effects and hardware non-idealities of actual continuous time (CT) signal generation. In this paper, we bridge this gap by developing a CT-analytical framework based on the affine Fourier series (AFS) representation, which allows us to demonstrate that strictly bandlimited pulses and subcarrier suppression strategies are essential to maintain the multicarrier structure of the signal. In addition, we derive the analytical power spectral density of AFDM and evaluate its spectral characteristics in comparison with other multicarrier schemes, considering the impact of realistic truncated pulse-shaping. Furthermore, we analyze the sensitivity of the CT model to phase noise, carrier frequency offset, and sampling jitter, providing a theoretical analysis of communication performance. Finally, we derive closed-form Cramér-Rao bounds for channel parameter estimation, showing that the chirped modulation peculiar of AFDM increases the estimation variance but enables the resolution of Doppler ambiguities. Our findings provide the necessary theoretical and practical foundations for the implementation of AFDM in realistic wireless transceivers.

Index terms— Affine frequency division multiplexing (AFDM), Cramér-Rao bound, continuous-time model, pulse-shaping, power spectral density, hardware impairment.

I. INTRODUCTION

The standardization of the sixth generation (6G) of public wireless networks is driven by the need to support extreme mobility scenarios, including high-speed railway systems, connected autonomous vehicles (CAV), low earth orbit (LEO) satellite constellations, unmanned aerial vehicles (UAVs), and more. In such environments, severe time-frequency (TF) dispersion, results in a doubly-selective (DS), or doubly-dispersive, fading profile, characterized by high Doppler shifts and multipath delays [1], [2], which have been recently investigated for a variety of 6G scenarios [3]–[5].

Authors are with: [‡]University of Modena and Reggio Emilia, Dept. of Engineering “Enzo Ferrari”, Via P. Vivarelli 10/1, 41125 Modena (Italy) Consorzio Nazionale Interuniversitario per le Telecomunicazioni (CNIT), and with [†]School of Computer Science and Engineering, Constructor University, 28759 Bremen, Germany. Emails: michele.mirabella@unimore.it, hrou@constructor.university, pasquale.diviesti@unimore.it, gabreu@constructor.university, giorgio.vitetta@unimore.it. Part of this work has been supported by the European Italian National Recovery and Resilience Plan (PNRR). Specifically the project has involved the MOST – Sustainable Mobility National Research Center.

Orthogonal frequency division multiplexing (OFDM), the cornerstone of fourth generation (4G) and fifth generation (5G) systems, is remarkably robust to frequency-selective fading but suffers significant performance degradation in high-mobility scenarios. In particular, DS channels result in loss of orthogonality among subcarriers, leading to inter-carrier interference (ICI) which complicates channel estimation and detection, significantly deteriorating the performance of OFDM [6]. To address these challenges, novel waveform designs have been proposed, such as the orthogonal time frequency space (OTFS) modulation, operating in the invariant delay-Doppler (DD) domain and demonstrating excellent robustness to the Doppler effects [7]–[9].

Recently, however, affine frequency division multiplexing (AFDM) has emerged as a flexible and promising alternative to OTFS [10]–[12], showing lower detection complexity and greater compatibility with OFDM [13], [14]. Based on the discrete affine Fourier transform (DAFT), AFDM employs chirp-periodic basis functions parameterized by a tunable chirp index. By optimally adjusting this chirp parameter, AFDM can align the signal representation with the Doppler profile of the channel, thus achieving full diversity and ensuring that multipath components remain separable in the affine Fourier domain (AFD) [15]. This property makes AFDM particularly attractive not only for communications but also for integrated sensing and communications (ISAC), as it efficiently allows for the estimation of delay and Doppler parameters [16].

Despite the growing body of literature on AFDM, the majority of existing studies rely exclusively on discrete time (DT), matrix-algebraic signal models. While sufficient for designing digital precoders or detectors [17], DT models fail to capture physical-layer (PHY) issues which may impact practical deployment, since, in real hardware, signals are generated and received in continuous time (CT). It is worth remarking that CT signal modeling has already shown its usefulness in the analysis of several digital modulation schemes available in the literature. In particular, exhaustive CT analyses have also been conducted for OFDM systems, where such an approach has led to a rigorous characterization of hardware impairments (HWIs), including pulse-shaping effects, inter-symbol interference (ISI) and ICI, synchronization errors, and phase noise (PN) [18], [19]. Other recent examples include the faster-than-Nyquist (FTN) variant of OFDM known as spectrally efficient frequency division multiplexing (SEFDM) [20], the precursor of AFDM, namely, orthogonal chirp divi-

sion multiplexing (OCDM) [21], frequency-modulated OFDM [22], and of course the more recent OTFS modulation.

Beyond interference and synchronization aspects, CT modeling has also proven to be a useful tool for the analysis of the peak behavior of OFDM signals. In this context [23] exploited a CT analytical framework to study the peak factor of multicarrier waveforms, highlighting limitations of DT representations. Moreover, [24] derived analytical bounds on the peak-to-mean envelope power ratio (PMEPR) as a function of the oversampling rate, and proposed some methods for peak power estimation together with associated error bounds.

In the context of FTN multicarrier schemes, a SEFDM variant that closely follows the OFDM transmission structure, employing a cyclic prefix (CP), root-raised cosine (RRC) pulse-shaping at the transmitter and the introduction of virtual carriers was recently proposed in [25], [26]. This design allows for a simple CT signal representation and significantly simplifies the receiver architecture, especially in terms of channel estimation and subsequent detection, while preserving the spectral efficiency gains of SEFDM over OFDM.

For OTFS, recent works such as [8], [9] have proposed CT frameworks that explicitly account for pulse-shaping and its impact on pilot placement and channel estimation performance. While [8] focuses on Zak-OTFS signaling based on TF localized waveforms (i.e., the so-called "pulsesones"), [9] adopts a multicarrier-based approach inspired by OFDM, employing a double CP (DCP) structure and RRC pulses to guarantee ISI-free reception in both time and frequency domains.

Similarly, for OCDM, the CT analysis presented in [27] has allowed the authors to highlight several non-ideal effects, including time-burst interference (TBI), narrowband interference (NBI), as well as to derive analytical expressions for the peak-to-average power ratio (PAPR).

Motivated by the above discussion, this paper develops a CT signal model for AFDM modulation, generated by following the typical implementation blocks used for multicarrier schemes. The framework highlights aspects which are often overlooked by DT formulations, including pulse-shaping aspect, receiver filtering, sampling, local oscillator (LO) impairments, and fractional delay and Doppler shifts, and their impact on AFDM orthogonality, performance bounds for communication, and channel parameter estimation. Furthermore, the CT model allows the analysis of implementation-related aspects, such as spectral occupancy, synchronization sensitivity, and the interplay between PN, carrier frequency offset (CFO), and channel time variations, thereby filling a relevant modeling gap in the AFDM literature and providing tools for realistic performance assessment and advanced transceiver design.

Our main contributions can be summarized as follows:

1) We provide, for the first time, a rigorous derivation of the AFDM waveform using a CT model based on the affine Fourier series (AFS). This framework is closer to physical reality than DT models from current AFDM literature and provides insights for fundamental limitations and real-world implementation.

2) We investigate the effects of pulse-shaping on the AFDM signal, identifying the RRC as the most suitable pulse. We

demonstrate analytically and through numerical examples why subcarrier suppression strategies are necessary to maintain the multicarrier signal structure.

2) We investigate the effects of pulse-shaping on the AFDM signal, identifying the RRC as the most suitable pulse. We derive the analytical expression of the power spectral density (PSD) of AFDM, evaluating it under realistic conditions such as pulse truncation. Furthermore, we provide a spectral comparison with other multicarrier schemes, highlighting how pulse-shaping and subcarrier suppression are necessary to maintain the multicarrier signal structure and control out-of-band (OOB) emissions. Despite the use of SCs, AFDM still achieves a higher throughput than OFDM in high-mobility channels, thanks to reduced pilot overhead and improved resilience to ICI, confirming the robustness of AFDM reported in the literature.

3) We extend the CT model to analyze the impact of realistic hardware impairments (HWIs), PN, CFO, and sampling jitter (SJ), which are often neglected in matrix-based DT models.

4) We derive the Cramér-Rao Bounds (CRBs) for delay and Doppler estimation in closed form, providing a theoretical benchmark for AFDM sensing performance in DS channels.

The rest of the manuscript is organized as follows. Section II introduces the fundamental CT derivation of the AFDM waveform based on the AFS. Section III investigates the analytical PSD, the impact of HWIs on the AFDM received signal, together with the theoretical bit-error-rate (BER) analysis and the derivation of the closed-form CRBs for delay and Doppler estimation in DS channels. Section IV presents numerical results and performance benchmarks to validate our analysis of AFDM, and finally, Section V concludes the paper.

Notation: Throughout this paper, superscripts $(\cdot)^*$ and $(\cdot)^H$ denote the complex conjugate and conjugate transpose (Hermitian), respectively. The operator $\text{mod}_B[\cdot]$ indicates the modulo B operation, while $*$ denotes the *linear convolution* between two signals or functions. For a complex variable x , we denote its *real* and *imaginary parts* as $\Re\{x\}$ and $\Im\{x\}$, respectively. We define a matrix $\mathbf{X} \triangleq [x_{m,n}]$, where $x_{m,n}$ represents the element in the m th row and n th column. \mathbf{I}_N denotes the *identity matrix* of order N , and $\mathbf{\Xi}_V$ represents the unitary discrete Fourier transform (DFT) matrix of order V , where the (p, q) th entry is given by $\exp(-j2\pi pq/V)/\sqrt{V}$. Finally, $\text{diag}(\mathbf{x}_N)$ denotes an $N \times N$ diagonal matrix with the elements of the N -dimensional vector \mathbf{x}_N on its main diagonal.

II. SYSTEM AND SIGNAL MODELS

In this section, we develop the CT analytical model for AFDM, starting from its DT formulation. The proposed derivation follows the same rules adopted for OFDM in [9, Sec. II-A], but it extends it to the AFD, thus providing a rigorous framework to investigate the physical interpretation, pulse-shaping effects and spectral properties of AFDM signals.

To this end, the section is organized into three parts. The first subsection presents the generation of the AFDM transmit signal, highlighting the role of the modulation parameters and the transmit pulse in shaping the chirp-periodic waveform. The second subsection derives the received signal model under

ideal, non-distorting channel conditions, illustrating the basic demodulation mechanism and its relationship with the DAFT. Finally, the third section extends the analysis to the case of a DS channel, characterized by both time and frequency dispersion.

A. Generation of AFDM Signals

Consider the transmission of an N -dimensional¹ information vector $\mathbf{c}_N \triangleq [c_0, c_1, \dots, c_{N-1}]^T$, whose entries are symbols drawn from an M_c -ary constellation. This vector represents one AFDM symbol and carries the information in the AFD. According to [10], the mapping between the AFD and the time domain (TD) is achieved through the inverse discrete affine Fourier transform (IDAFT) with parameters (λ_1, λ_2) as

$$\mathbf{x}_N = \mathbf{A}_{\lambda_1, \lambda_2}^H \mathbf{c}_N, \quad (1)$$

where

$$\mathbf{A}_{\lambda_1, \lambda_2} \triangleq \mathbf{\Lambda}_{\lambda_2} \mathbf{\Xi}_N \mathbf{\Lambda}_{\lambda_1} \quad (2)$$

is the DAFT matrix, and

$$\mathbf{\Lambda}_{\lambda} \triangleq \text{diag}(\mathbf{a}_{N, \lambda}), \quad (3)$$

where $\mathbf{a}_{N, \lambda} \triangleq [a_{\lambda, 0}, \dots, a_{\lambda, N-1}]^T$ and $a_{\lambda, n} \triangleq \exp(-j2\pi\lambda n^2)$.

It is easy to show that the n th element of \mathbf{x}_N , in (1), can be expressed as

$$x_n = \frac{1}{\sqrt{N}} \sum_{m=0}^{N-1} c_m \exp(j2\pi(\lambda_1 n^2 + \lambda_2 m^2 + mn/N)), \quad (4)$$

for which the *chirp periodicity property*

$$x_{n+lN} = x_n \exp(j2\pi\lambda_1(l^2 N^2 + 2nlN)), \quad (5)$$

holds for any choice of indices (l, n) .

Moreover, the *inverse chirp periodicity property*

$$c_{m+lN} = c_m \exp(-j2\pi\lambda_2(l^2 N^2 + 2mlN)), \quad (6)$$

also holds, for any pair of indices (m, l) .

In order to obtain a CT waveform, the vector \mathbf{x}_N in (1) is periodically extended, yielding the chirp-periodic sequence \bar{x}_k , so that $\bar{x}_k = x_k$ for any $k \in \{0, 1, \dots, N-1\}$ and

$$\bar{x}_k = x_{\text{mod}_N[k]} \exp(j2\pi\lambda_1(N^2 + 2Nk)), \quad (7)$$

holds for any $k \notin \{0, 1, \dots, N-1\}$.

As shown in Fig. 2, the phase $\angle\{\bar{x}_k\}$ of the AFDM sequence repeats every N samples, illustrating the DT chirp-periodic extension of the original vector \mathbf{x}_N . The OFDM phase, obtained from the same quadrature amplitude modulation (QAM) symbols with $\lambda_1 = \lambda_2 = 0$, is also shown as a reference, highlighting the effect of the chirp-periodic modulation on the phase evolution.

The sequence $\{\bar{x}_k\}$ feeds a pulse amplitude modulator, which produces the baseband signal

$$s(t; \mathbf{c}_N) = \sum_{k=-\infty}^{+\infty} \bar{x}_k p(t - kT_s) \exp(-j2\pi\lambda_1 k^2) \exp(j2\pi\bar{\lambda}_1 t^2), \quad (8)$$

where $\bar{\lambda}_1 = \lambda_1/T_s^2$ is the chirp parameter in Hz^2 .

¹An even value of N is assumed in this paper.

In (8), it is important to observe that: 1) the resulting signal is chirp-periodic with period $T \triangleq NT_s$, since

$$s(t + T; \mathbf{c}_N) = s(t; \mathbf{c}_N) \exp(j2\pi\bar{\lambda}_1(T^2 + 2Tt)), \quad (9)$$

and 2) the quadratic phase terms in (8) compensate and induce the time-varying frequency characteristic of AFDM signals.

Fig. 1 illustrates the magnitude and phase of the CT AFDM-signal generated from the chirp-periodic sequence $\{\bar{x}_k\}$. The OFDM signal, obtained from the same QAM symbols (with $\lambda_1 = \lambda_2 = 0$) is shown as a reference. Vertical dashed lines correspond to multiples of the period T , highlighting the chirp-periodicity of the AFDM signal. As expected from (8), the AFDM phase evolves quadratically within each period, showing the time-varying frequency characteristic induced by the quadratic phase terms, whereas the OFDM phase remains piecewise constant over each symbol period.

Because of its chirp-periodicity, which is obtained, in practice, through the insertion of a chirp-periodic prefix (CPP) of length N_{cpp} [10], the signal in (8) admits the AFS representation (see App. A)

$$s(t; \mathbf{c}_N) = \sum_{m=-\infty}^{+\infty} S_m(\mathbf{c}_N) \exp(j2\pi(\bar{\lambda}_1 t^2 + \frac{m}{T}t)), \quad (10)$$

holding in the interval $[0, T]$; here

$$S_m(\mathbf{c}_N) = \frac{1}{T} \int_0^T s(t; \mathbf{c}_N) \exp(-j2\pi(\bar{\lambda}_1 t^2 + \frac{m}{T}t)) dt, \quad (11)$$

is the m th coefficient of such series, which embeds the information vector \mathbf{c}_N and the effect of pulse-shaping.

Substituting the right-hand side (RHS) of (8) into that of (11), reorganizing the summations, and using the property in (5), one obtains, after simple manipulations,

$$S_m(\mathbf{c}_N) = \frac{1}{\sqrt{NT_s}} c_m P_m \exp(j2\pi\lambda_2 m^2), \quad (12)$$

where $P_m \triangleq P(m\Delta_f)$, $\Delta_f \triangleq 1/(NT_s)$ is the *subcarrier spacing* and $P(f)$ denotes the continuous Fourier transform (CFT) of the pulse $p(t)$.

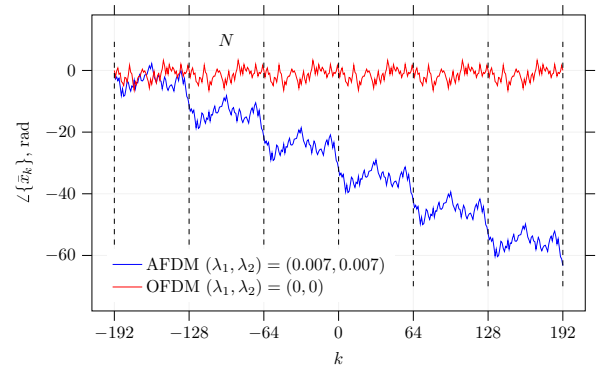


Figure 2. Unwrapped phase of the DT sequences $\{\bar{x}_k\}$ for both AFDM and OFDM, generated from the same 4-QAM symbols. Vertical dashed lines indicate multiples of the symbol period $N = 64$. AFDM parameters $\lambda_1 = \lambda_2 = 0.007$ are used for the chirp-periodic sequence. The OFDM curve ($\lambda_1 = \lambda_2 = 0$) is included for comparison.

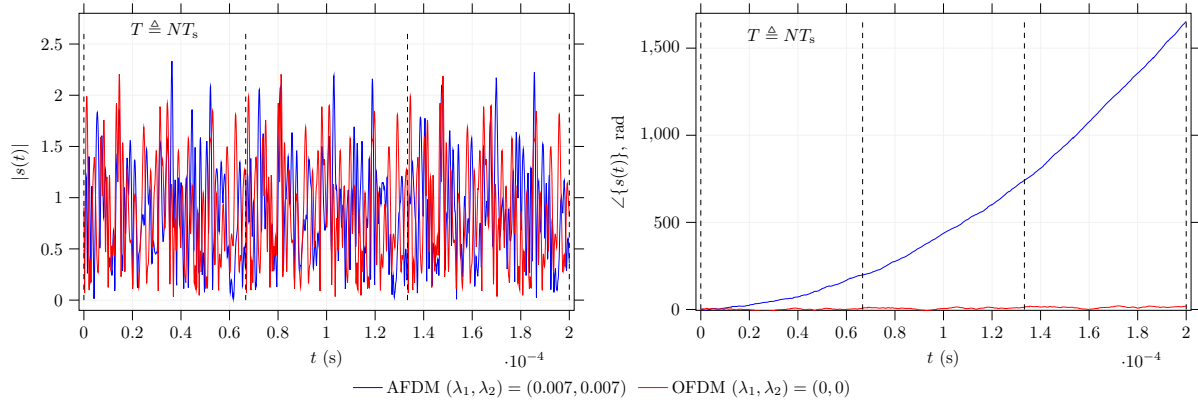


Figure 1. Magnitude (left) and unwrapped phase (right) of the CT AFDM (with $\lambda_1 = \lambda_2 = 0.007$) and OFDM signals generated from the same 4-QAM symbols over multiple periods. Vertical dashed lines indicate the signal period T . The following parameters have been employed for generating the CT signals: 1) $N = 64$; 2) RRC pulse $p(t)$ with roll-off factor $\alpha = 0.15$; 3) oversampling factor $N_c = 10$; 4) $T_s = 1.04 \mu\text{s}$.

Replacing (12) in (10) yields the CT AFDM signal model

$$s(t; \mathbf{c}_N) = \frac{1}{\sqrt{NT_s}} \sum_{m=-\infty}^{+\infty} c_m P_m \exp(j2\pi\lambda_2 m^2) \cdot \exp\left(j2\pi\left(\bar{\lambda}_1 t^2 + \frac{m}{T}t\right)\right). \quad (13)$$

By expressing $m = q + kN$ with $q \in [-N/2, N/2 - 1]$, for any k and using (6), (13) becomes

$$s(t; \mathbf{c}_N) = \frac{1}{\sqrt{N}T_s} \sum_{q=-N/2}^{N/2} c_{\text{mod}_N[q]} \exp(j2\pi\lambda_2 q^2) \cdot \exp\left(j2\pi\left(\bar{\lambda}_1 t^2 + \frac{q}{T}t\right)\right) \sum_{k=-\infty}^{+\infty} P_{q+kN} \exp\left(j2\pi\frac{k}{T_s}t\right). \quad (14)$$

As in conventional OFDM [18, Sec. 3.7.2], waveform deployments rely on *strictly bandlimited* transmit (TX) pulses to generate a structured multicarrier signal, which force the sum over k in (14) to vanish. As a result, the residual spectral replicas do not overlap with the useful band, thereby preventing self-interference (SI). In practice, a RRC pulse is often employed. Owing to its *excess bandwidth*, only a subset $N_u < N$ of subcarriers can be used without SI. The remaining $N_{\text{sc}} = N - N_u$ subcarriers are therefore intentionally deactivated, hereafter referred to as suppressed carriers (SCs).

If the roll-off factor is α , the number of active subcarriers is $N_u = 2N_\alpha + 1$, with $N_\alpha \triangleq \lfloor N(1 - \alpha)/2 \rfloor$. Therefore, the finite and infinite sums appearing in the RHS of (14) involve only N_u useful terms and a single term, respectively, so that (14) can be expressed as

$$s(t; \mathbf{c}_N) = \frac{1}{\sqrt{N}T_s} \sum_{m=-N_\alpha}^{N_\alpha} c_{\text{mod}_N[m]} P_{\text{mod}_N[m]} \cdot \exp(j2\pi\lambda_2 m^2) \exp\left(j2\pi\left(\bar{\lambda}_1 t^2 + \frac{m}{T}t\right)\right). \quad (15)$$

B. Receive Signal Model of AFDM Under Ideal Communication Channels

We consider the signal $s(t; \mathbf{c}_N)$, in (15), is sent over an ideal communication channel, so that the signal available at the receiver is $z(t; \mathbf{c}_N) = s(t; \mathbf{c}_N)$.

Such signal feeds the receive (RX) filter, whose impulse response (IR) is $g(t) = u(-t) \exp(j2\pi\bar{\lambda}_1 t^2)$, with $u(t)$ being a real signal. Then, the response

$$r(t; \mathbf{c}_N) \triangleq z(t; \mathbf{c}_N) * g(t), \quad (16)$$

becomes

$$r(t; \mathbf{c}_N) = \frac{1}{\sqrt{N}T_s} \sum_{m=-N_\alpha}^{N_\alpha} c_{\text{mod}_N[m]} P_{\text{mod}_N[m]} \cdot U^*\left(2\bar{\lambda}_1 t + \frac{m}{N T_s}\right) \exp\left(j2\pi\left(\bar{\lambda}_1 t^2 + \frac{m}{T}t + \lambda_2 m^2\right)\right), \quad (17)$$

with $U(f)$ being the CFT of $u(t)$.

As it can be observed from the last result, the RX filtering results into the introduction of a factor $U(\cdot)^*$, sampled at a time-dependent instant and also depending on the index m . Again, note that, when $\lambda_1 = 0$ (i.e., $\bar{\lambda}_1 = 0$), $U(\cdot)$ is sampled at a fixed frequency $f_m = m/T$, as it occurs for OFDM.

The signal $r(t; \mathbf{c}_N)$ (17) is sampled at the instants $t_{\tilde{n}} \triangleq \tilde{n}T_s$ (with $\tilde{n} = 0, 1, \dots, N + N_{\text{cpp}} - 1$). It is easy to show that the \tilde{n} th sample $\tilde{r}_{\tilde{n}} \triangleq r(t_{\tilde{n}}; \mathbf{c}_N)$, after removing the CPP (i.e., $\tilde{n} = 0, 1, \dots, N - 1$), can be expressed as

$$\tilde{r}_{\tilde{n}} = \frac{1}{\sqrt{N}T_s} \sum_{m=-N_\alpha}^{N_\alpha} c_{\text{mod}_N[m]} P_{\text{mod}_N[m]} U^*\left(2\frac{\lambda_1}{T_s}\tilde{n} + \frac{m}{N T_s}\right) \cdot \exp\left(j2\pi\left(\lambda_1 \tilde{n}^2 + \frac{m}{N}\tilde{n} + \lambda_2 m^2\right)\right). \quad (18)$$

This last result shows that, differently from OFDM, in AFDM the RX pulse depends also on the sampling instant through \tilde{n} . In order to proceed further in the derivations we need to select the normalized chirp parameter and the RX pulse bandwidth properly. Regarding the first parameter, we select it as [10] $\lambda_1 = A/(2N)$, with $A \in \mathbb{Z}$. As regards the RX pulse, its spectrum shall be *strictly bandlimited* and, in particular we require that

$$U^*(f_{\tilde{n},m}) = \begin{cases} \sqrt{T_s} & |f_{\tilde{n},m}| \leq B_{\text{rx}}/2, \\ 0 & |f_{\tilde{n},m}| > B_{\text{rx}}/2, \end{cases} \quad (19)$$

with $f_{\tilde{n},m} \triangleq (A\tilde{n} + m)\Delta_f$ and B_{rx} being the RX pulse bandwidth.

It is easy to prove that by selecting 1) $A = 1$ and 2) $B_{\text{rx}} = [2N(1 + \alpha)]\Delta_f$, then $U^*(f_{\tilde{n},m}) = \sqrt{T_s}$ for any $\tilde{n} \in \{0, 1, \dots, N-1\}$ and any $m \in \{-N_\alpha, -N_\alpha + 1, \dots, -1, 0, 1, \dots, N_\alpha\}$. This allows us to express (18) as

$$\check{r}_{\tilde{n}} \triangleq r(t_{\tilde{n}}; \mathbf{c}_N) = \frac{1}{\sqrt{N}} \sum_{m=-N_\alpha}^{N_\alpha} c_{\text{mod}_N[m]} \cdot \exp\left(j2\pi\left(\lambda_1 \tilde{n}^2 + \frac{m}{N} \tilde{n} + \lambda_2 m^2\right)\right), \quad (20)$$

provided that $P_{\text{mod}_N[m]} = \sqrt{T_s}$ for each considered m .

Storing the sequence $\{\check{r}_{\tilde{n}}; \tilde{n} = 0, 1, \dots, N-1\}$ into the N -dimensional vector

$$\mathbf{r}_N \triangleq [\check{r}_0, \check{r}_1, \dots, \check{r}_{N-1}]^T = \mathbf{A}_{\lambda_1, \lambda_2}^H \mathbf{c}_N, \quad (21)$$

immediately shows that \mathbf{c}_N can be obtained from \mathbf{r}_N by applying an order N DAFT, with parameters (λ_1, λ_2) , to the vector \mathbf{r}_N , so that

$$\mathbf{y}_N \triangleq [y_0, y_1, \dots, y_{N-1}]^T = \mathbf{A}_{\lambda_1, \lambda_2} \mathbf{r}_N = \mathbf{c}_N. \quad (22)$$

C. Receive Signal Model of AFDM in DS Channels

Let us focus now on the reception on a linear time-variant (LTV) multipath fading channel characterized by channel impulse response (CIR)

$$h(t, \tau) = \sum_{l=0}^{L-1} h_l(t, \tau), \quad (23)$$

where

$$h_l(t, \tau) \triangleq a_l \exp(j2\pi\nu_l t) \delta(\tau - \tau_l), \quad (24)$$

denotes the l th path contribution, while a_l , τ_l and ν_l represent the gain, the delay² and the Doppler shift associated with the l th channel path, respectively, and L is the overall number of paths.

We first consider the contribution of the l th channel path $h_l(t, \tau)$ (see (24)) to the RX signal after RX filtering as

$$r_l(t; \mathbf{c}_N) = s(t; \mathbf{c}_N) * h_l(t, \tau) * g(t), \quad (25)$$

where the additive noise term was neglected for simplicity.

It is not difficult to prove that the last signal can be alternatively expressed as

$$\begin{aligned} r_l(t; \mathbf{c}_N) &= \frac{\tilde{a}_l}{\sqrt{NT_s}} \sum_{m=-N_\alpha}^{N_\alpha} c_{\text{mod}_N[m]} P_{\text{mod}_N[m]} \exp(j2\pi\lambda_2 m^2) \\ &\cdot \exp\left(-j2\pi\frac{m}{T}\tau_l\right) U^*\left(2\bar{\lambda}_1(t - \tau_l) + \frac{m}{T} + \nu_l\right) \\ &\cdot \exp\left(j2\pi\left(\bar{\lambda}_1 t^2 + \frac{m}{T}t\right)\right) \exp(j2\pi(\nu_l - 2\bar{\lambda}_1\tau_l)t), \end{aligned} \quad (26)$$

where $\tilde{a}_l \triangleq a_l \exp(j2\pi\bar{\lambda}_1\tau_l^2) \exp(-j2\pi\nu_l\tau_l)$.

²We assume the CIR components are arranged in ascending order of delays, so that τ_0 and τ_{L-1} are the minimum and maximum delays, respectively.

After 1) sampling the last signal at the instants $t_{\tilde{n}} \triangleq \tau_{L-1} + \tilde{n}T_s$ and 2) following the same rules employed to evaluate (20), one obtains

$$\begin{aligned} \bar{r}_{l, \tilde{n}} &= \frac{\tilde{a}_l}{\sqrt{NT_s}} \sum_{m=-N_\alpha}^{N_\alpha} c_{\text{mod}_N[m]} P_{\text{mod}_N[m]} \bar{U}_m^* \\ &\cdot \exp\left(j2\pi\left(\lambda_1 \tilde{n}^2 + \frac{m}{N} \tilde{n} + \lambda_2 m^2\right)\right) \\ &\cdot \exp(j2\pi m F_{\tau_l}) \exp\left(j2\pi\left(F_{\nu_l}/N + 2\lambda_1 N F_{\tau_l}\right) \tilde{n}\right), \end{aligned} \quad (27)$$

where,

$$\tilde{a}_l \triangleq \tilde{a}_l \exp(j2\pi\bar{\lambda}_1\tau_{L-1}^2) \exp(j2\pi(\nu_l - 2\bar{\lambda}_1\tau_l)\tau_{L-1}), \quad (28)$$

$$F_{\tau_l} \triangleq \frac{\tau_{L-1} - \tau_l}{NT_s}, \quad (29)$$

$$F_{\nu_l} \triangleq \nu_l/\Delta_f, \quad (30)$$

respectively denote the complex gain, the normalized delay and the normalized Doppler frequency associated³ with the l th channel path.

In order to account for all the channel paths we sum $\bar{r}_{l, \tilde{n}}$ (27) over l as follows

$$\check{r}_{\tilde{n}} \triangleq \sum_{l=0}^{L-1} \bar{r}_{l, \tilde{n}}. \quad (31)$$

Then, the sequence $\{\check{r}_{\tilde{n}}; \tilde{n} = 0, 1, \dots, N-1\}$ is stored into the N -dimensional vector

$$\mathbf{r}_N \triangleq [\check{r}_0, \check{r}_1, \dots, \check{r}_{N-1}]^T, \quad (32)$$

and undergoes order N DAFT processing, with parameters (λ_1, λ_2) , thus obtaining

$$\mathbf{y}_N \triangleq [y_0, y_1, \dots, y_{N-1}]^T = \mathbf{A}_{\lambda_1, \lambda_2} \mathbf{r}_N. \quad (33)$$

The last vector can be expressed, including additive white Gaussian noise (AWGN), as

$$\mathbf{y}_N = \mathbf{H} \mathbf{c}_N + \mathbf{w}_N, \quad (34)$$

where $\mathbf{H} \triangleq [H_{m,n}]$ denotes the $N \times N$ effective channel matrix and $\mathbf{w}_N \triangleq [w_0, w_1, \dots, w_{N-1}]^T$ is the AWGN vector affecting \mathbf{y}_N .

In particular the (m, n) th coefficient of the effective channel matrix \mathbf{H} , in (34), can be expressed as

$$\begin{aligned} H_{m,n} &= \frac{1}{T_s} P_m \bar{U}_m^* \exp(j2\pi\lambda_2(m^2 - n^2)) \\ &\cdot \sum_{l=0}^{L-1} \tilde{a}_l \exp(j2\pi m F_{\tau_l}) \mathcal{F}_l[n - m], \end{aligned} \quad (35)$$

where

$$\mathcal{F}_l[x] = G_N\left(F_{\nu_l}/N + 2\lambda_1 N F_{\tau_l} - x/N\right), \quad (36)$$

is the term describing the nature of ICI in AFDM modulation (for a given index x), whereas

$$G_X(\theta) \triangleq \frac{1}{X} \frac{\exp(-j2\pi\theta X) - 1}{\exp(-j2\pi\theta) - 1}, \quad (37)$$

is the *Dirichlet kernel* of order X and phase θ . A characterization of the channel matrix \mathbf{H} is provided in App. C.

³In obtaining (27), $|NF_{\tau_l}| < N$ and $|NF_{\nu_l}| < N$ have been assumed $\forall l$.

III. POWER SPECTRAL DENSITY, RECEIVER IMPAIRMENTS, AND FUNDAMENTAL BOUNDS OF AFDM

In this section, we analyze the performance of AFDM signals from both a signal characterization and a communication & sensing perspectives. In particular, we first evaluate the PSD of the TX AFDM signal to highlight its spectral properties, which are affected by the chirp parameters and the pulse-shaping. Then, we investigate the impact of three different receiver impairments listed in Tab. I, namely, we consider PN, CFO, and SJ, aiming at showing how these non-idealities affect the communication performance. An evaluation of the theoretical BER achieved with an linear minimum mean square error (LMMSE) receiver is then provided, offering further insight into the robustness of AFDM in the presence of HWIs and DS channels. Finally, we derive the CRB for the estimation of channel delay and Doppler shifts, providing fundamental limits for sensing performance. This latter part complements the communication analysis by showing how well AFDM can estimate channel parameters compared to OFDM, and how the chirp parameter λ_1 influences the theoretical bounds.

A. Power Spectral Density of TX AFDM Signals

In this subsection, we evaluate the PSD for AFDM modulation. We rewrite the modulated signal $s(t; \mathbf{c}_N)$, in (8), as

$$s(t; \mathbf{c}_N) = \sum_{k=-N_{\text{cpp}}}^{N-1} \bar{x}_k p(t - kT_s) \exp(j2\pi(\bar{\lambda}_1 t^2 - \lambda_1 k^2)), \quad (38)$$

where the infinite sum appearing in the RHS of (8) has been replaced by the finite counterpart.

Following [18], the evaluation of the PSD for an AFDM signal can be done according to the three following steps: 1) evaluation of the average PSD of the data sequence $\{x_k\}$; 2) application of [18, Eq. (3.66)], employed for the evaluation of the PSD of a pulse amplitude modulation (PAM) signal, to the evaluation of the PSD of an AFDM signal.

In our derivations we assume that the $N_u = 2N_\alpha + 1$ useful elements of the channel symbol vector \mathbf{c}_N are such that: a) they belong to an M_c -ary constellation; b) they are statistically independent and identically distributed (i.i.d.), with zero mean and variance σ_c^2 . This last assumption implies that the sequence $\{\bar{x}_k\}$ collects i.i.d. terms, thanks to the orthogonality property of the IDAFT transform in (1).

We begin by computing the PSD of the sequence $\{\bar{x}_k\}$. Since the sequence contains statistically i.i.d. terms only, the average PSD of such sequence is (see [18, Eq. (3.287)])

$$\bar{S}_x(f) = \frac{\sigma_c^2}{N N_T} \sum_{l=-N_\alpha}^{N_\alpha} \frac{\sin^2(\pi N_T(f - f_l)T_s)}{\sin^2(\pi(f - f_l)T_s)}, \quad (39)$$

where $N_T \triangleq N + N_{\text{cpp}}$ and $f_l = l/(NT_s)$ is the frequency of the l th subcarrier of the baseband AFDM signal.

Table I

RECEIVER IMPAIRMENTS CONSIDERED IN OUR AFDM ANALYSIS.

Impairment	References	System model
Phase Noise	[28], [29]	DT
Carrier Frequency Offset	[28], [29]	DT
Sampling Jitter	-	-

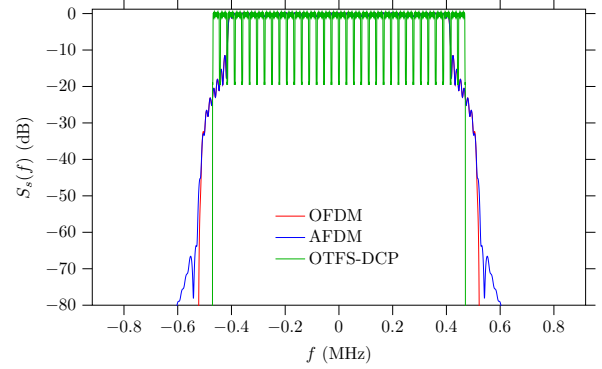


Figure 3. Normalized PSD of OFDM, AFDM ($\lambda_1 = \lambda_2 = 0.007$) and OTFS-DCP. All the considered waveforms occupy the same bandwidth $B = 1$ MHz and use $N = 64$ subcarriers. The size of the OTFS-DCP modulation is $M \times N$, with $M = 32$, it employs the same ideal (untruncated) RRC pulse $p(t)$ adopted for OFDM and AFDM, with roll-off factor $\alpha = 0.15$ and FD CP and a postfix of sizes $N_{\text{cp}}^{(\text{FD})} = N_{\text{cpo}}^{(\text{FD})} = 1$, respectively.

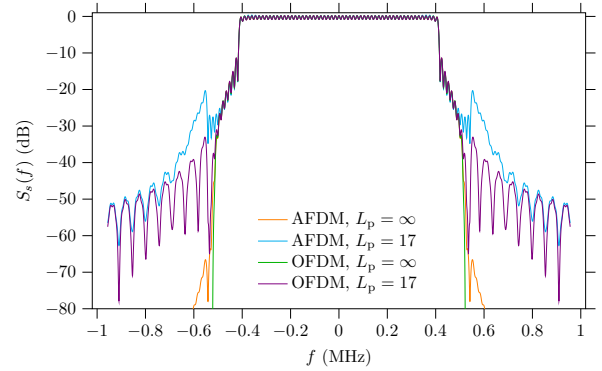


Figure 4. Normalized PSD of OFDM and AFDM signals for ideal (untruncated, $L_p = \infty$) and truncated ($L_p = 17$) pulse-shaping. For AFDM, $\lambda_1 = \lambda_2 = 0.007$ have been assumed.

Therefore, the average PSD of $s(t, \mathbf{c}_N)$ (38) is given by

$$S_s(f) = \frac{1}{T_s} \bar{S}_x(f) |P(f) * W(f)|^2, \quad (40)$$

with⁴

$$W(f) = \frac{1}{\sqrt{\lambda_1}} \exp\left(-j\pi \frac{f^2}{2\lambda_1}\right) \frac{1+j}{2}. \quad (41)$$

Fig. 3 compares the PSDs of OFDM, AFDM, and OTFS-DCP (normalized with respect to the factor $\sigma_c^2/(N N_T)$) under the same bandwidth constraint ($B = 1$ MHz) and number of subcarriers ($N = 64$). The size of the OTFS-DCP modulation is $M \times N$, with $M = 32$, and the same ideal RRC pulse $p(t)$, with $\alpha = 0.15$, adopted for OFDM and AFDM.

As expected, AFDM exhibits a spectral behavior that deviates from OFDM due to the introduction of the chirp factor λ_1 , which alters the orthogonality structure in the frequency domain (FD). In general, increasing the chirp parameter results in a broader spectral occupation and higher OOB emissions.

For OTFS-DCP, the additional FD CP and postfix generate visible spectral components outside the nominal band. However, these frequency guard bands are removed at the receiver through filter-bank sampling, as discussed in [9].

⁴Note that, when $\lambda_1 = 0$, then $W(f) = \delta(f) \forall f$, i.e., it coincides with the Dirac delta function.

Fig. 4 highlights the impact of pulse truncation on spectral containment for both OFDM and AFDM. When an ideal (non-truncated) pulse is considered (so that the truncation order $L_p = \infty$ is considered), both OFDM and AFDM exhibit similar OOB behavior, with such levels equal to -40 dB and -39.24 dB, respectively. This demonstrates that, under ideal conditions, the two waveforms provide comparable spectral confinement. However, when the pulse is truncated to $L_p = 17$, the spectral leakage increases for both schemes. In particular, the OOB level degrades to -37 dB for OFDM and -30 dB for AFDM. While OFDM experiences a moderate degradation (approximately 3 dB), AFDM shows approximately a 3 times higher OOB emissions. This behavior suggests that AFDM is more sensitive to pulse truncation effects, which can be attributed to the additional chirp modulation introduced by the parameter λ_1 .

B. Receive Signal Model for AFDM with PN, CFO and DS Channel

In this section, we extend the AFDM signal model to DS channels in the presence of PN and CFO at the receiver. For such analysis, we assume both PN and CFO vary slowly over one sampling interval T_s .

Under the above considered impairments, the l th component of the RX signal filtered by the DS channel, and after RX matched filtering can be expressed as

$$r_l(t; \mathbf{c}_N)^{(\text{PN+CFO})} = \left((s(t; \mathbf{c}_N) * h_l(t, \tau)) \cdot \exp(j\phi(t) + j2\pi f_{\text{cfo}} t) \right) * g(t), \quad (42)$$

where $\phi(t)$ denotes a real-valued stochastic process⁵ accounting for the PN introduced by the RX LO, while f_{cfo} represents the CFO at the receiver.

After RX filtering and sampling at $t_{\tilde{n}} = \tau_{L-1} + \tilde{n}T_s$ (with $\tilde{n} = 0, 1, \dots, N-1$), the \tilde{n} th sample, corresponding to the l th channel path contribution, can be expressed as

$$\begin{aligned} \bar{r}_{l,\tilde{n}} \triangleq r_l(t_{\tilde{n}}; \mathbf{c}_N) &\cong \frac{\check{a}_l}{\sqrt{NT_s}} \sum_{m=-N_\alpha}^{N_\alpha} c_{\text{mod}_N[m]} P_{\text{mod}_N[m]} U_m^* \\ &\cdot \exp(j2\pi m F_{\tau_l}) \exp\left(j2\pi \left(\lambda_1 \tilde{n}^2 + \frac{m}{N} \tilde{n} + \lambda_2 m^2\right)\right) \\ &\cdot \exp\left(j2\pi \left((F_{\nu_l} + F_{\text{cfo}})/N + 2\lambda_1 N F_{\tau_l}\right) \tilde{n}\right) \exp(j\phi_{\tilde{n}}), \end{aligned} \quad (43)$$

with $\check{a}_l = \check{a} \exp(j2\pi f_{\text{cfo}} \tau_{L-1})$, and where $F_{\text{cfo}} \triangleq f_{\text{cfo}}/\Delta_f$ is the CFO normalized with respect to Δ_f , whereas $\phi_{\tilde{n}} \triangleq \phi(\tilde{n}T_s)$ represents the \tilde{n} th sample of the PN process.

In order to account for all the channel paths we sum $\bar{r}_{l,\tilde{n}}$ (43) over l to obtain $\check{r}_{\tilde{n}} \triangleq \sum_{l=0}^{L-1} \bar{r}_{l,\tilde{n}}$. Then, the sequence $\{\check{r}_{\tilde{n}}; \tilde{n} = 0, 1, \dots, N-1\}$ is stored into the N -dimensional vector $\mathbf{r}_N \triangleq [\check{r}_0, \check{r}_1, \dots, \check{r}_{N-1}]^T$ and undergoes order N DAFT processing, with parameters (λ_1, λ_2) , thus obtaining

$$\mathbf{y}_N \triangleq [y_0, y_1, \dots, y_{N-1}]^T = \mathbf{A}_{\lambda_1, \lambda_2} \mathbf{r}_N. \quad (44)$$

⁵The random process $\phi(t)$ is often modeled as a slowly varying *Wiener process*, whose increments are independent Gaussian random variables [30].

To proceed further: 1) we include AWGN samples $\{w_n; n = 0, 1, \dots, N-1\}$, characterized by variance σ_w^2 , in the model above and 2) we linearize the discrete process $\phi_{\tilde{n}}$, so that $\phi_{\tilde{n}} \cong \bar{\phi}_0 + \tilde{n}T_s \bar{\phi}_1$, where $(\bar{\phi}_0, \bar{\phi}_1)$ represent the coefficients of the first-order polynomial approximation of the discrete PN process. Therefore, the vector \mathbf{y}_N can be expressed as

$$\mathbf{y}_N = \mathbf{H}^{(\text{PN+CFO})} \mathbf{c}_N + \mathbf{w}, \quad (45)$$

where $\mathbf{H}^{(\text{PN+CFO})} \triangleq [H_{m,n}^{(\text{PN+CFO})}]$ denotes the *effective channel matrix* including PN and CFO impairments. In fact, its (m, n) th element can be expressed as

$$H_{m,n}^{(\text{PN+CFO})} = \frac{1}{T_s} P_m U_m^* \exp(j2\pi \lambda_2 (m^2 - n^2)) \sum_{l=0}^{L-1} \check{a}_l \exp(j2\pi m F_{\tau_l}) \mathcal{Q}_l[n-m], \quad (46)$$

where $\check{a}_l \triangleq \check{a}_l \exp(j\bar{\phi}_0)$ and (see (37)) $\mathcal{Q}_l[x] = G_N((F_{\nu_l} + F_{\text{cfo}})/N + 2\lambda_1 N F_{\tau_l} - x/N + \bar{\phi}_1/2\pi)$ for any integer x .

C. Receive Signal Model for AFDM with SJ and DS Channel

In this subsection, we analyze the impact of SJ on the RX AFDM signal in the presence of a DS channel. To this end, we first consider the signal $r_t(t; \mathbf{c}_N)$, in (26), to be sampled at the instants

$$t_{\tilde{n}}^{(\text{sj})} \triangleq \tau_{L-1} + \tilde{n}T_s + \delta_{\text{sj}}(\tilde{n}T_s), \quad (47)$$

with $\tilde{n} = 0, 1, \dots, N-1$; here $\delta_{\text{sj}}(\cdot)$ is a real-valued stochastic process modeling the SJ and representing a deviation from the ideal sampling grid.

In our analysis we assume the SJ process to be sufficiently small that it can be linearized as

$$\delta_{\text{sj}}(\tilde{n}T_s) = \bar{\delta}_0 + \tilde{n}T_s \bar{\delta}_1, \quad (48)$$

where $\bar{\delta}_0$ represents a constant timing offset, while $\bar{\delta}_1$ models a sampling clock skew.

Under this last assumption, the \tilde{n} th sample of the RX signal, referred to the l th channel path, can be expressed as

$$\begin{aligned} \bar{r}_{l,\tilde{n}}^{(\text{sj})} &\cong \frac{\check{a}_l}{\sqrt{NT_s}} \sum_{m=-N_\alpha}^{N_\alpha} c_{\text{mod}_N[m]} P_{\text{mod}_N[m]} U_m^* \\ &\cdot \exp(j2\pi m F_{\tau_l}) \exp\left(j2\pi \left(\lambda_1 \tilde{n}^2 + \frac{m}{N} \tilde{n} + \lambda_2 m^2\right)\right) \\ &\cdot \exp\left(j2\pi \left(F_{\nu_l}^{(\text{sj})}/N + 2\lambda_1 N F_{\tau_l}^{(\text{sj})}\right) \tilde{n}\right), \end{aligned} \quad (49)$$

where $\check{a}_l \triangleq \check{a}_l \exp(j2\pi(\nu_l - 2\bar{\lambda}_1 \tau_l) \bar{\delta}_0)$, $F_{\nu_l}^{(\text{sj})} \triangleq F_{\nu_l}(1 + \bar{\delta}_1)$ and $F_{\tau_l}^{(\text{sj})} \triangleq (\tau_{L-1} - \tau_l(1 + \bar{\delta}_1))/(NT_s)$.

To account for the L channel paths, we evaluate the RX signal $\check{r}_{\tilde{n}}^{(\text{sj})} = \sum_{l=0}^{L-1} \bar{r}_{l,\tilde{n}}^{(\text{sj})}$. Then, the RX vector $\mathbf{r}_N^{(\text{sj})} \triangleq [\check{r}_0^{(\text{sj})}, \check{r}_1^{(\text{sj})}, \dots, \check{r}_{N-1}^{(\text{sj})}]^T$ is constructed. This undergoes an order N DAFT, with parameters (λ_1, λ_2) , thus producing

$$\mathbf{y}_N^{(\text{sj})} \triangleq \mathbf{A}_{\lambda_1, \lambda_2} \mathbf{r}_N^{(\text{sj})} = \mathbf{H}^{(\text{sj})} \mathbf{c}_N + \mathbf{w}_N, \quad (50)$$

with $\mathbf{H}^{(\text{sj})} \triangleq [H_{m,n}^{(\text{sj})}]$ being an $N \times N$ effective channel matrix, whose (m, n) th element is

$$H_{m,n}^{(sj)} = \frac{1}{T_s} P_m U_m^* \exp(j2\pi\lambda_2(m^2 - n^2)) \cdot \sum_{l=0}^{L-1} \check{a}_l \exp(j2\pi m F_{\tau_l}) \mathcal{K}_l[n - m], \quad (51)$$

where $\mathcal{K}_l[x] = G_N(F_{\nu_l}^{(sj)}/N + 2\lambda_1 N F_{\tau_l}^{(sj)} - x/N)$ for any index x (see (37)), represents the ICI term corrupted by SJ.

D. Bit-error-rate Analysis under LMMSE Detection

Based on the effective channel matrix \mathbf{H} derived in the previous subsections, which can account for the combined effects of pulse-shaping, multipath DS channel and HWI, we evaluate the AFDM system performance in terms of BER when deploying a LMMSE detector. Given the RX signal model, in the form of (34), the LMMSE detector estimates the TX symbol vector \mathbf{c}_N as

$$\hat{\mathbf{c}}_N \triangleq [\hat{c}_0, \hat{c}_1, \dots, \hat{c}_{N-1}]^T = \mathbf{G}_{\text{lmmse}} \mathbf{y}_N, \quad (52)$$

where

$$\mathbf{G}_{\text{lmmse}} \triangleq [G_{m,n}^{(\text{lmmse})}] \triangleq (\mathbf{H}^H \mathbf{H} + \sigma_w^2 \mathbf{I}_N)^{-1} \mathbf{H}^H \quad (53)$$

is the $N \times N$ LMMSE equalization matrix.

The n th element of (52) can be expressed as

$$\hat{c}_n = \bar{G}_{n,n} c_n + \sum_{k \neq n} \bar{G}_{n,k} c_k + \bar{w}_n, \quad (54)$$

where $\bar{G}_{n,k}$ is the element (n, k) of the $N \times N$ matrix $\bar{\mathbf{G}} \triangleq [\bar{G}_{n,k}] = \mathbf{G}_{\text{lmmse}} \mathbf{H}$, with both the indices n and k varying from 0 to $N - 1$.

Note that, in (54), the term \bar{w}_n is the n th element of the vector $\bar{\mathbf{w}}_N \triangleq \mathbf{G}_{\text{lmmse}} \mathbf{w}_N$. It is not difficult to show that the signal-to-interference-plus-noise ratio (SINR) associated with the estimated symbol \hat{c}_n can be expressed as

$$\text{SINR}_n = \frac{\bar{G}_{n,n}}{1 - \bar{G}_{n,n}}. \quad (55)$$

Then, the approximate average BER, BER_{av} , evaluated for the considered LMMSE equalized vector $\hat{\mathbf{c}}_N$ (52), collecting symbols belonging to a QAM constellation, can be formulated as [31, Sec. 4.3, Eq. (4.3-30)]

$$\text{BER}_{\text{av}} \cong \frac{1}{N} \frac{4}{\log_2(M_c)} \left(1 - \frac{1}{\sqrt{M_c}}\right) \sum_{n=0}^{N-1} Q\left(\sqrt{\frac{3 \text{SINR}_n}{M_c - 1}}\right), \quad (56)$$

where $Q(\cdot)$ denotes the Gaussian Q-function, which can be tightly bounded [32], yielding a closed form expressions for the approximate BER.

E. Cramér-Rao Bounds on AFDM Channel Parameter Estimation Errors

In this subsection, we derive the CRBs for the estimation of normalized delay and Doppler in an AFDM-based communication system. The CRB provides a fundamental performance benchmark for unbiased estimators and is here used to assess the sensing capability of AFDM waveforms.

We first consider the RX signal model in (34) and focus on the estimation of channel delay and Doppler. To obtain closed-form expressions, we restrict the analysis to a single path channel ($L = 1$). The resulting bounds also act as lower bounds for the multipath case.

The following assumptions are adopted throughout the derivation: 1) the received signal is affected by AWGN with variance σ_w^2 ; 2) the vector \mathbf{c}_N contains $N_u \leq N$ non-zero symbols, drawn independently from a phase-shift keying (PSK) or a QAM constellation with variance σ_c^2 ; 3) the transmit symbols satisfy $\mathbb{E}\{\mathbf{c}_N \mathbf{c}_N^H\} = (N_u/N) \sigma_c^2 \mathbf{I}_N$; 4) the channel consists of a single DD component (i.e., $L = 1$), namely, (F_τ, F_ν) with unknown deterministic amplitude \bar{a} ; 5) a symmetric FD pulse and SCs are employed.

Let $\boldsymbol{\psi} = [F_\tau, F_\nu]^T$ denote the vector collecting normalized delay and Doppler. For AWGN observations, the 2×2 Fisher information matrix (FIM) associated with the ML estimator is given by [33]

$$\boldsymbol{\Upsilon} \triangleq [\nu_{m,n}] = 2\Re \left\{ \frac{\partial \tilde{\mathbf{y}}}{\partial \boldsymbol{\psi}} \left(\frac{\partial \tilde{\mathbf{y}}}{\partial \boldsymbol{\psi}} \right)^H \right\}, \quad (57)$$

where $\tilde{\mathbf{y}} = \mathbf{H} \mathbf{c}_N$ denotes the noiseless received signal.

Exploiting the above assumptions, the (k, k') th entry of the FIM, in (57), can be expressed as

$$\nu_{k,k'} = 2 \frac{N_u}{N} \sigma_c^2 \text{Tr} \left\{ \frac{\partial \mathbf{H}}{\partial \psi_k} \left(\frac{\partial \mathbf{H}}{\partial \psi_{k'}} \right)^H \right\}. \quad (58)$$

The closed form expression of the CRB associated with the estimation of delay and Doppler can be achieved by: 1) computing the partial derivatives in (58) for all (k, k') index combinations; 2) substituting them into the FIM expression; 3) approximating the geometric series terms arising from point 2) by retaining only the dominant contributions; 4) inverting the resulting FIM; and 5) extracting its diagonal entries. In doing so, closed-form expressions for the CRBs are obtained after further approximation by retaining dominant terms only. Their resulting closed form expressions are then

$$\text{CRB}_{F_\tau} \cong \frac{1}{2\pi^2 \sigma_c^2 \text{SNR} N_u \left(\frac{N_u}{3} - 2\lambda_1^2 (N - 2)^2\right)}, \quad (59)$$

and

$$\text{CRB}_{F_\nu} \cong \frac{N_u}{3\pi^2 \sigma_c^2 \text{SNR} N_u \left(\frac{N_u}{3} - 2\lambda_1^2 (N - 2)^2\right)}, \quad (60)$$

where the signal-to-noise ratio (SNR) is defined as $\text{SNR} \triangleq |\bar{a}|^2 / \sigma_w^2$. The obtained CRB expressions deserve the following comments.

- 1) When $\lambda_1 = 0$, the CRB values refer to OFDM.
- 2) The two expressions are defined and valid for $0 \leq \lambda_1 \leq \sqrt{N_u}/(\sqrt{6}(N - 2))$. Note that, since λ_1 is typically selected to be approximately $1/(2N)$ [10], the aforementioned condition is met for values of $N \geq 16$.
- 3) In general, introducing a non-zero chirp parameter λ_1 in AFDM leads to a degradation of the theoretically achievable estimation performance for both delay and Doppler, as indicated by the corresponding CRBs. In fact, when $\lambda_1 = 0$, i.e., in the OFDM case, one obtains lower

variance of unbiased estimation. However, it is important to note that these OFDM performance levels are purely theoretical: in practice, especially in multipath scenarios, conventional estimators are unable to separate different Doppler components in OFDM, making the obtained bound unattainable. In contrast, AFDM (i.e., $\lambda_1 \neq 0$) enables separating Doppler multipath components, allowing estimators to approach its theoretical performance, despite the higher related CRB value.

IV. NUMERICAL RESULTS

In this section, we assess the performance of the proposed CT AFDM framework through a set of numerical simulations. To this end, we start by investigating the impact of pulse-shaping on AFDM signal generation. Different TX pulses are considered and the subcarrier suppression mechanism is shown. Since the pulse shape, as well as the use of SC directly affects the FIM associated with delay and Doppler parameters, we also report the corresponding CRBs for normalized delay and Doppler frequency estimation.

Subsequently, we compare the theoretical BER performance achieved by LMMSE detection when employing the channel model, derived from our CT analysis, with that obtained using the DT-based model commonly adopted in the literature. The comparison is carried out under two DS channel scenarios: 1) varying maximum channel path velocity, and 2) varying the overall number of channel paths. This allows us to highlight the impact of fractional delays, pulse-shaping, and Doppler modeling accuracy on detection performance.

Finally, we evaluate the robustness of the proposed AFDM communication system in the presence of HWI, namely, PN, CFO, and SJ. The resulting BER curves are compared with those achieved by OFDM under identical detection and DS channel conditions, thereby quantifying the relative resilience of the two modulation schemes in more realistic scenarios.

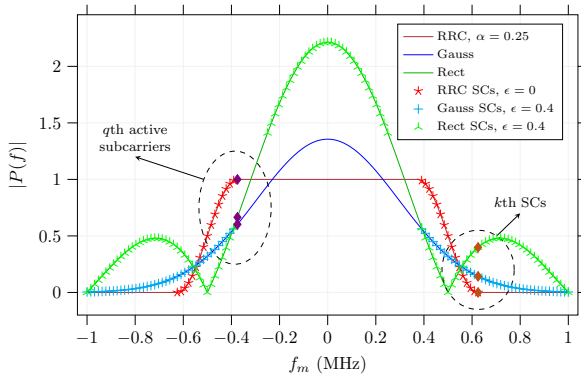


Figure 5. Magnitude spectrum of the pulses selected for AFDM signal generation. The RRC, Gaussian and rectangular pulses have been considered. The AFDM signal is characterized by a useful bandwidth $B = 1$ MHz and $N = 64$ subcarriers. Markers indicate the position of the SCs, so that only $N_u = N - N_{sc}$ useful subcarriers are retained.

Our first results, illustrated by Figs. 5 and 6, focus on the impact of pulse-shaping on AFDM signal generation and on the corresponding estimation-theoretic limits.

For such analysis, the following simulation settings are adopted. An M_c -PSK constellation is employed so that $\sigma_c^2 = 1$ independently of M_c . The number of subcarriers is $N = 64$,

the subcarrier spacing is $\Delta_f = 15$ kHz, the AFDM chirp parameter is $\lambda_1 = 0.007$, and, for the RRC pulse, the roll-off factor is $\alpha = 0.25$. All considered pulses (RRC, Gaussian, and rectangular) are designed to occupy approximately the same bandwidth $B \simeq 1$ MHz; for the rectangular and Gaussian pulses, the 3-dB bandwidth (i.e., main lobe) is considered.

Fig. 5 shows the magnitude spectra of the adopted pulses together with the position of the AFDM subcarriers. It can be observed that only the RRC pulse exhibits a flat-top frequency response over its useful band, whereas the Gaussian and rectangular pulses do not. As a consequence, when the RRC pulse is employed, all active subcarriers are weighted uniformly in frequency, while this property cannot be ensured for the other two pulses.

The SC mechanism explained in Sec. II-A is applied in order to prevent SI. For RRC pulses, the number of suppressed subcarriers is determined by the roll-off factor, leading to $N_u = 2N_\alpha + 1$ useful subcarriers. In turn, for Gaussian and rectangular pulses, the absence of a flat-top region requires introducing a positive tolerance parameter, here fixed to $\epsilon = 0.4$, to determine which subcarriers can be retained.

As highlighted in Fig. 5, the subcarrier frequencies are indexed by $m = q + kN$, consistently with (14). This representation clearly shows that, when shifting the q th active subcarrier (see purple diamonds Fig. 5) by multiples of N , either the corresponding spectral replica must be suppressed or the pulse spectrum must be null at that frequency (see, for instance brown diamonds, relative to SCs, in Fig. 5). Otherwise, the summation over k in (14) would not reduce to a single term, and the resulting waveform would no longer exhibit a multicarrier structure. Therefore, strict band-limitation (or an equivalent SC mechanism) is essential to preserve the multicarrier nature of the AFDM signal. Among the considered pulses, the RRC provides the most favorable behavior thanks to its flat-top region.

Fig. 6 shows the CRBs for the estimation of normalized delay and Doppler frequencies obtained with the three considered pulse shapes. From that figure, several observations can be made.

1) The RRC pulse, employed for AFDM, consistently achieves the lowest CRB values for both delay and Doppler estimation over the entire SNR range. This is a direct consequence of its flat-top frequency response, which ensures uniform subcarrier weighting and maximizes the useful number of samples N_u .

2) For the same tolerance ϵ , the Gaussian pulse outperforms the rectangular one. The smoother spectral decay of the Gaussian pulse provides a more favorable distribution of spectral energy across the retained subcarriers, resulting in improved estimation accuracy.

3) Increasing the tolerance ϵ enlarges the number of useful subcarriers N_u , thereby increasing the number of signal samples contributing to delay and Doppler estimation.

4) The CRBs associated with OFDM are very close to that of AFDM when employing the same RRC pulse setting. In particular, OFDM achieves slightly tighter bounds, improving delay and Doppler estimation by less than 1% and 3%, respectively. It is worth emphasizing that this advantage is purely

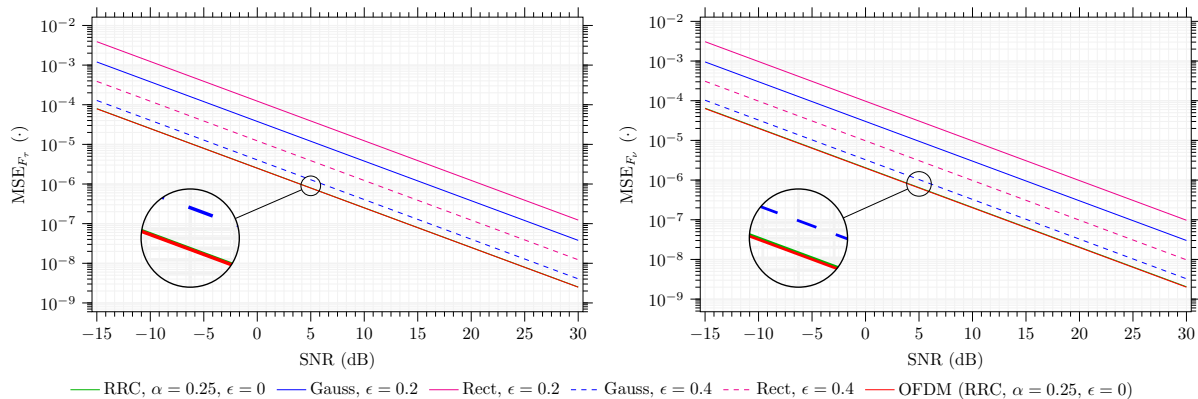


Figure 6. Theoretical CRB for the estimation of normalized delay and Doppler frequencies in AFDM modulation, generated with three different pulses (namely, RRC, Gaussian and rectangular) using SC mechanism to limit or avoid SI. An SNR $\in [-15, 30]$ dB has been considered. The CRBs achieved by OFDM (i.e., $\lambda_1 = \lambda_2 = 0$) employing RRC pulse with $\alpha = 0.25$ are also shown for comparison.

theoretical and holds only under single-path (i.e., $L = 1$) conditions; in multipath scenarios, OFDM is generally unable to separate the different path contributions, whereas AFDM preserves resolvability.

Table II
PARAMETERS OF AFDM EMPLOYED IN SIMULATIONS.

Parameter	Value
# subcarriers	$N = 64$
AFDM chirp parameters	$\lambda_1 = \lambda_2 = 0.007$
CPP length	$N_{\text{cpp}} = 4$
Pulse-shaping	RRC, with $\alpha = 0.25$
Carrier frequency	$f_c = 5.8$ GHz
Subcarrier spacing	$\Delta f = 15$ kHz

This leads to improved (i.e., lower) CRB values. However, this improvement is only theoretical. The CRB derivation assumes AWGN with identical statistics across subcarriers. When non-flat pulses are used, the retained subcarriers are scaled by different spectral magnitudes of the pulse, thus inducing non-uniform noise statistics across samples. Hence, the AWGN assumption underlying the CRB no longer holds.

In conclusion, the RRC pulse emerges as the most suitable choice among the considered candidates and, more generally, pulses exhibiting a flat-top frequency response are preferable for AFDM modulation, as they simultaneously guarantee SI mitigation and uniform subcarrier weighting for improved parameter estimation performance.

In this subsection, we compare the BER performance obtained using the proposed CT channel model with that derived from the DT formulation commonly adopted in the literature.

The AFDM signals are generated using only the RRC pulse and the system parameters are reported in Tab. II.

The wireless channel is assumed to be DS: its The Doppler spectrum is generated according to the Jakes' model, with maximum Doppler spread determined by the maximum channel path velocity v_{max} . The power delay profile (PDP) and the associated path delays follow the *tapped delay line* model of type A (TDL-A) [34].

Fig. 7 illustrates the BER⁶ performance of AFDM under

⁶All BER curves are obtained by averaging over 100 independent Monte Carlo channel realizations using the analytical expression in (56).

LMMSE detection for different maximum channel path velocities $v_{\text{max}} \in \{0, 50, 150, 300, 450\}$ km/h.

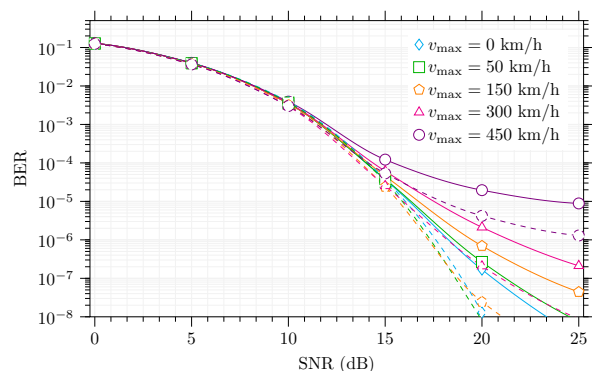


Figure 7. Bit-error rate achieved by AFDM LMMSE detection under a DS channel with $L = 3$ paths and various maximum velocities $v_{\text{max}} \in \{0, 50, 150, 300, 450\}$ km/h. Solid lines refer to the use of the CT model-based channel matrix, while dashed lines employ its DT model-based counterpart. SNR $\in [0, 25]$ dB is considered.

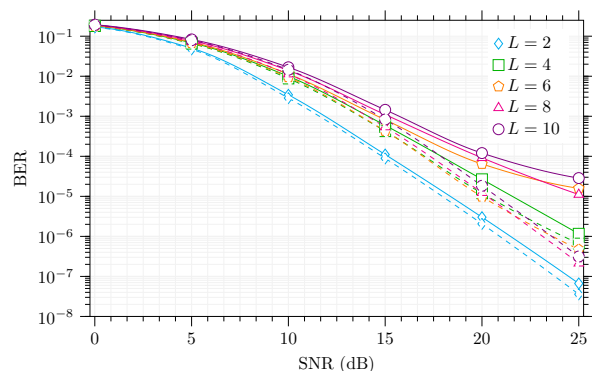


Figure 8. Bit-error rate achieved by AFDM LMMSE detection under a DS channel with variable number of paths $L \in \{2, 4, 6, 8, 10\}$. Solid lines refer to the use of the CT model-based channel matrix, while dashed lines employ its DT model-based counterpart. SNR $\in [0, 25]$ dB is considered.

A comparison is provided between the channel matrix derived from the proposed CT model (solid lines) and that obtained from the DT model (dashed lines). As expected, BER performance degrades as v_{max} increases due to the larger Doppler spread, which enhances time selectivity and ICI. More importantly, the BER values predicted by the CT model are consistently higher than those obtained with the DT model. The resulting gap highlights a fundamental limitation of DT-

based models, which neglect both pulse-shaping impact and fractional delays and consider only fractional Doppler shifts.

Fig. 8 illustrates the BER performance of AFDM as a function of SNR $\in [0, 25]$ dB for different numbers⁷ of channel paths $L \in \{2, 4, 6, 8, 10\}$, with $v_{\max} = 250$ km/h.

Increasing the number of channel paths L results in a progressive BER degradation. A larger L implies a richer multipath structure and enhanced DD dispersion, thus worsening detection performance. Once again, the BER values obtained with the more accurate CT model are consistently higher than those achieved by the DT model for every considered value of L across the entire SNR range.

The latter confirms that the DT formulation systematically underestimates the impact of multipath components and fractional effects in the DS channel.

Next, we evaluate the robustness of AFDM compared to OFDM in the presence of HWI, specifically PN, CFO, and SJ. To ensure a fair comparison, both modulations employ the same LMMSE detection scheme.

The simulations are conducted over a DS channel, whose PDP follows a TDL-A channel model with $L = 3$ paths, a delay spread of $0.5 \mu\text{s}$, and a maximum velocity $v_{\max} = 250$ km/h. All impairment processes are modeled as zero-mean Gaussian distributions with standard deviations (stds) denoted by σ_ϕ , σ_{CFO} , and σ_{SJ} , respectively.

Fig. 9 illustrates the impact of PN on the system performance. From the results, it can be easily inferred that AFDM significantly outperforms OFDM across all considered values of σ_ϕ . While OFDM suffers from a severe error floor even at low PN levels due to both common phase error and Doppler-induced ICI, AFDM maintains a performance close to the case where no PN is present for $\sigma_\phi \leq 0.01$, demonstrating superior robustness to phase instabilities.

Fig. 10 shows the BER as a function of SNR for different CFO stds. It is easy to verify that OFDM performance degrades rapidly as the CFO increases, with the BER saturating at values above 10^{-3} for $\sigma_{\text{CFO}} \geq 10^{-7}$ ppm. Conversely, AFDM better handles the frequency offsets; even at the highest considered impairment (10^{-5} ppm), AFDM achieves a BER near 10^{-7} at 25 dB, whereas OFDM fails to provide reliable communication in the same SNR range.

Fig. 11 illustrates the system performance in the presence of SJ. It can be observed that both modulations are relatively robust to the variability of the SJ itself, as the curves within each group (solid or dashed) remain closely bundled. The substantially higher BER of OFDM compared to AFDM is mainly due to the Doppler-induced ICI from the DS channel, rather than the SJ itself. Interestingly, AFDM appears more sensitive to SJ variations than OFDM, as evidenced by the wider spread between its curves at high SNR values (above 20 dB). This increased sensitivity can be attributed to the chirp-based nature of the AFDM waveform.

⁷As L increases, the overall delay spread generally enlarges according to the adopted TDL-A profile, leading to increased frequency selectivity.

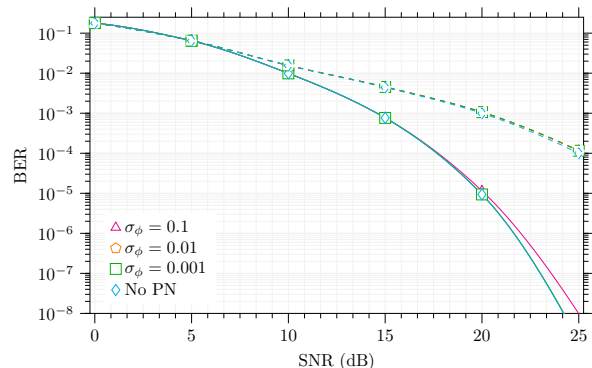


Figure 9. Average BER under PN for AFDM (solid lines) and OFDM (dashed lines) with $\sigma_\phi \in \{0, 0.001, 0.01, 0.1\}$. An SNR $\in [0, 25]$ dB is considered.

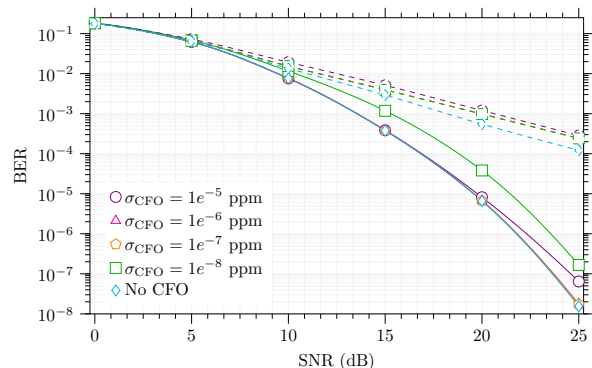


Figure 10. Average BER under CFO for AFDM (solid lines) and OFDM (dashed lines). The CFO stds are expressed in ppm relative to the carrier frequency f_c . An SNR $\in [0, 25]$ dB is considered.

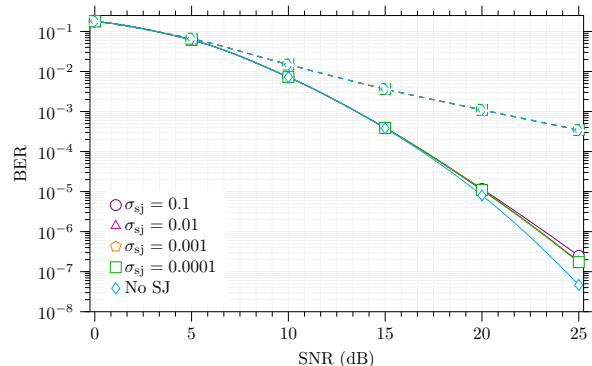


Figure 11. Average BER under SJ for AFDM (solid lines) and OFDM (dashed lines) with $\sigma_{\text{SJ}} \in \{0.1, 0.01, 0.001, 0.0001\}$. An SNR $\in [0, 25]$ dB is considered.

V. CONCLUSIONS

We presented a comprehensive CT analytical framework for AFDM modulation. By bridging the gap between theoretical DT models and physical hardware constraints, we revealed that AFDM requires carefully designed pulse-shaping and subcarrier suppression to preserve its multicarrier properties. For instance, the analysis of the PSD has shown that although AFDM shares spectral similarities with OFDM, the choice of pulse-shaping and the impact of pulse truncation are more critical tasks for controlling OOB, due to the additional chirp modulation inherent of AFDM. Our study of HWIs, including PN, CFO, and SJ, further demonstrates, however, that although not impervious to these effects AFDM maintains a significant resilience compared to conventional OFDM in high-mobility channels, thereby confirming the literature claims on

such format. The derivation of closed-form CRBs for delay and Doppler estimation highlights a fundamental trade-off. In particular, although AFDM exhibits a higher theoretical estimation variance than OFDM due to its additional chirp modulation, it enables the resolution of Doppler ambiguities in multipath environments. These results provide useful tools for the design and realistic performance assessment of next-generation wireless communication systems.

Future work will focus on developing channel estimation and data detection strategies based on the proposed CT model. Such methods are expected to enable more efficient pilot design and AFDM receiver architectures and to shed new light into AFDM feasibility over state-of-the-art implementations.

APPENDIX

A. Properties of AFS and Continuous AFT

In this appendix, we summarize the main properties and characteristics of the AFS and the continuous affine Fourier transform (AFT), which generalize classical Fourier transforms for chirp-periodic signals.

Let $s(t)$ be a chirp-periodic signal with chirp period T and chirp parameter $\bar{\lambda}_1$, such that, for the given T , $s(t+T) = s(t) \exp(j2\pi\bar{\lambda}_1(T^2 + 2Tt))$, holds for any t .

Then, the AFS expansion of $s(t)$ is $s(t) = \sum_{m=-\infty}^{+\infty} S_m \psi_m(t)$, where the basis functions are, for any m ,

$$\psi_m(t) = \exp\left(j2\pi\left(\bar{\lambda}_1 t^2 + \frac{m}{T}t\right)\right), \quad (61)$$

and the coefficients are obtained by projection

$$S_m = \frac{1}{T} \int_0^T s(t) \psi_m^*(t) dt. \quad (62)$$

Note that the AFS reduces to the classical Fourier series (FS) when $\bar{\lambda}_1 = 0$. Moreover, the basis functions $\psi_m(t)$, in (61), are orthogonal over one chirp period, i.e., $\int_0^T \psi_m(t) \psi_n^*(t) dt = 0$, for $m \neq n$.

The continuous AFT generalizes the CFT to signals with quadratic phase. The operation, dependent on the parameter λ_1 , can be written as

$$S_{\lambda_1}(f) = \int_{-\infty}^{+\infty} s(t) \exp(-j2\pi(\bar{\lambda}_1 t^2 + ft)) dt. \quad (63)$$

This last operation maps a chirp-modulated TD signal into a domain where DD characteristics are separated. Moreover, it reduces to the classical CFT when $\bar{\lambda}_1 = 0$. It is also worth noting that the AFT of a sum of signals is the sum of their AFTs (i.e., it exhibits the *linearity* property). Finally, the inversion formula is

$$s(t) = \int_{-\infty}^{+\infty} S_{\lambda_1}(f) \exp(j2\pi(\bar{\lambda}_1 t^2 + ft)) df. \quad (64)$$

B. Convolution of a signal with a chirp-exponential

In this appendix we concentrate on the response of a signal $p(t)$ to a chirp-exponential function of the type

$$u(t) \triangleq \exp\left(j2\pi\left(\bar{\lambda}_1 t^2 + \frac{m}{T}t\right)\right). \quad (65)$$

In particular, we consider the linear convolution

$$y(t) = p^*(-t) * u(t) = \int_{-\infty}^{+\infty} p(-\tau) u(t-\tau) d\tau, \quad (66)$$

which after substituting $u(t-\tau)$ and expanding the quadratic phase gives

$$\begin{aligned} y(t) &= \int_{-\infty}^{+\infty} p(-\tau) \exp\left(j2\pi\left(\bar{\lambda}_1(t-\tau)^2 + \frac{m}{T}(t-\tau)\right)\right) d\tau \quad (67) \\ &= \exp\left(j2\pi\left(\bar{\lambda}_1 t^2 + \frac{m}{T}t\right)\right) \\ &\quad \cdot \int_{-\infty}^{+\infty} p(-\tau) \exp\left(j2\pi\left(\bar{\lambda}_1 \tau^2 - 2\bar{\lambda}_1 t\tau - \frac{m}{T}\tau\right)\right) d\tau. \end{aligned}$$

Now we change variable $\sigma = -\tau$ (note $d\tau = -d\sigma$ and integration limits remain $(-\infty, \infty)$); thus we obtain

$$\begin{aligned} y(t) &= \exp\left(j2\pi\left(\bar{\lambda}_1 t^2 + \frac{m}{T}t\right)\right) \quad (68) \\ &\quad \cdot \int_{-\infty}^{+\infty} p(\sigma) \exp\left(j2\pi\left(\bar{\lambda}_1 \sigma^2 + \left(2\bar{\lambda}_1 t + \frac{m}{T}\right)\sigma\right)\right) d\sigma. \end{aligned}$$

Denoting the m th time varying frequency by $f_m(t) \triangleq 2\bar{\lambda}_1 t + m/T$ and recalling the definition of the AFT, we obtain $y(t) = u(t) P_{\lambda_1}^*(f_m(t))$.

Therefore, the convolution with the chirp-exponential is not a time-invariant filtering in the usual sense, since the output is the chirp-exponential $u(t)$ multiplied by the AFT of $p(t)$ evaluated along the *time-varying* frequency argument $f_m(t)$.

C. Impulse Response Characterization of AFDM DS Channel

To provide further insight into the structure of the effective AFDM channel matrix $\mathbf{H} \triangleq [H_{m,n}]$ (see (35)) derived in Sec. II-C, we adopt an IR-based representation in the AFD.

In particular, we characterize the effective channel by evaluating its response to a discrete Dirac delta in the AFDM as

$$\mathbf{h}^{(\text{IR})} \triangleq [h_0^{(\text{IR})}, h_1^{(\text{IR})}, \dots, h_{N-1}^{(\text{IR})}]^T = \mathbf{H} \boldsymbol{\delta}_N, \quad (69)$$

where $\boldsymbol{\delta}_N$ is the N -dimensional Dirac vector, whose entries are all zero except for a single non-zero element⁸ equal to one.

Note that the vector $\mathbf{h}^{(\text{IR})}$, in (69), provides insights of how the energy of an isolated AFDM impulse spreads across that domain due to the combined effect of the DS channel and the AFDM modulation. Through this representation it is possible to highlight: 1) the path localization properties of the effective channel in the AFD; 2) the Doppler-induced ICI profile; 3) the impact of the chirp parameter λ_1 on the dispersion of the CIR.

⁸Without loss of generality, the non-zero element is placed at the central index, i.e., $n = \lfloor N/2 \rfloor$.

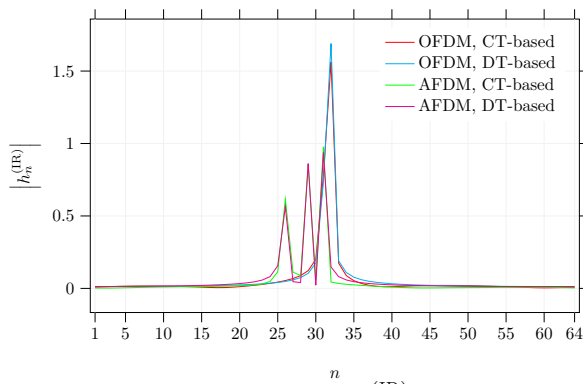


Figure 12. Magnitude of the AFDM IR $|h_n^{(IR)}|$ for OFDM and AFDM effective channel matrices obtained from CT-based and DT-based signal models.

Moreover, the same IR-based characterization can be easily extended to AFDM channel matrices that include receiver HWIs. In this case, the corresponding AFDM IR provides an insight of how such impairments affect energy spreading and coupling in the AFD.

The IRs $\mathbf{h}^{(IR)}$ obtained from both the proposed CT-based model and the DT-based AFDM formulation are illustrated in Fig. 12 for a single realization of a DS channel consisting of $L = 3$ propagation paths with delay taps τ_{bin} equal to 1.1 (including fractional delays), 3 and 6 and a Doppler spectrum following a Jakes model with maximum Doppler shift $\nu_{max} = 12$ kHz⁹. The parameters used to generate the numerical results shown in Fig. 12 are summarized in Tab. II. The plots reported in Fig. 12 show the magnitude of the AFDM IRs for both AFDM and OFDM (where $\lambda_1 = \lambda_2 = 0$).

From that Figure, the following comments can be made: 1) the CT-based and DT-based IRS closely match for both AFDM and OFDM, confirming the consistency of the CT formulation adopted in this work; 2) compared to OFDM, AFDM exhibits a more structured spreading of energy across AFD indices, induced by the chirp modulation and captured by the Dirichlet kernel terms in the effective channel matrix; 3) the curves associated with OFDM show the IRs in the conventional FD, where the 3 paths cannot be easily separated.

REFERENCES

- [1] C.-X. Wang *et al.*, “6G Wireless Channel Measurements and Models: Trends and Challenges,” *IEEE Veh. Technol. Mag.*, vol. 15, no. 4, pp. 22–32, Dec. 2020.
- [2] D. W. Bliss and S. Govindasamy, *Dispersive and doubly dispersive channels*. Cambridge University Press, 2013, pp. 341–364.
- [3] K. R. R. Ranasinghe *et al.*, “Doubly-Dispersive MIMO Channels With Stacked Intelligent Metasurfaces: Modeling, Parametrization, and Receiver Design,” *IEEE Trans. Wireless Commun.*, vol. 25, Sep. 2025.
- [4] —, “Flexible intelligent metasurfaces in high-mobility MIMO integrated sensing and communications,” *arXiv:2507.18793*, 2025.
- [5] —, “Doubly-Dispersive Continuous MIMO Systems: Channel Modeling and Beamforming Design,” *arXiv preprint arXiv:2509.00964*, 2025.
- [6] T. Wang, J. Proakis, E. Masry, and J. Zeidler, “Performance degradation of OFDM systems due to Doppler spreading,” *IEEE Trans. Wireless Commun.*, vol. 5, no. 6, pp. 1422–1432, Jun. 2006.
- [7] Z. Wei *et al.*, “Orthogonal time-frequency space modulation: A promising next-generation waveform,” *IEEE Wireless Commun.*, vol. 28, no. 4, pp. 136–144, Aug. 2021.

⁹According to the parameters listed in Tab. II, this value corresponds to a maximum path velocity $v_{max} \cong 1120$ km/h.

- [8] S. K. Mohammed *et al.*, “OTFS-Predictability in the Delay-Doppler Domain and Its Value to Communication and Radar Sensing,” *IEEE BITS Inform. Theory Mag.*, vol. 3, no. 2, pp. 7–31, Jun. 2023.
- [9] M. Mirabella, P. Di Vestì, and G. M. Vitetta, “On the Use of a Two-Dimensional Cyclic Prefix in OTFS Modulation and Its Implications,” *IEEE Open J. Commun. Soc.*, vol. 5, pp. 3340–3367, May 2024.
- [10] A. Bemani, N. Ksairi, and M. Kountouris, “Affine Frequency Division Multiplexing for Next Generation Wireless Communications,” *IEEE Trans. Wireless Commun.*, vol. 22, no. 11, pp. 8214–8229, Nov. 2023.
- [11] Q. Li *et al.*, “Affine Frequency Division Multiplexing for 6G Networks: Fundamentals, Opportunities, and Challenges,” *IEEE Netw.*, vol. 40, no. 1, pp. 88–97, Jan. 2026.
- [12] H. S. Rou *et al.*, “Affine Frequency Division Multiplexing (AFDM) for 6G: Properties, Features, and Challenges,” *IEEE Commun. Standards Mag.*, pp. 1–10, 2025.
- [13] —, “From Orthogonal Time-Frequency Space to Affine Frequency-Division Multiplexing: A comparative study of next-generation waveforms for integrated sensing and communications in doubly dispersive channels,” *IEEE Signal Process. Mag.*, vol. 41, no. 5, pp. 71–86, 2024.
- [14] —, “AFDM: Evolving OFDM Towards 6G+,” *arXiv:2602.08163*, 2026.
- [15] Y. Tao *et al.*, “Affine Frequency Division Multiplexing With Index Modulation: Full Diversity Condition, Performance Analysis, and Low-Complexity Detection,” *IEEE J. Sel. Areas Commun.*, vol. 43, no. 4, pp. 1041–1055, Jan. 2025.
- [16] Y. Luo *et al.*, “A Novel Angle-Delay-Doppler Estimation Scheme for AFDM-ISAC System in Mixed Near-Field and Far-Field Scenarios,” *IEEE Internet Things J.*, vol. 12, no. 13, pp. 22 669–22 682, Apr. 2025.
- [17] K. R. R. Ranasinghe, H. Seok Rou, G. Thadeu Freitas de Abreu, T. Takahashi, and K. Ito, “Joint Channel, Data, and Radar Parameter Estimation for AFDM Systems in Doubly-Dispersive Channels,” *IEEE Trans. Wireless Commun.*, vol. 24, no. 2, pp. 1602–1619, 2025.
- [18] G. M. Vitetta *et al.*, *Wireless communications: algorithmic techniques*. John Wiley & Sons, 2013.
- [19] U. Mengali, *Synchronization techniques for digital receivers*. Springer Science & Business Media, 2013.
- [20] M. S. Sarwar, I. N. A. Ramatryana, M. Ahmad, and S. Y. Shin, “Dual-mode index modulation for non-orthogonal frequency division multiplexing,” *IEEE Trans. Wireless Commun.*, vol. 22, no. 11, 2023.
- [21] G. Cuzzo, N. Longhi, and G. Pasolini, “Characterization of orthogonal chirp division multiplexing and performance evaluation at the frequencies in the presence of phase noise,” *IEEE Open J. Commun. Soc.*, vol. 5, pp. 238–255, 2024.
- [22] G. Romano *et al.*, “Investigating frequency modulated OFDM (FM-OFDM): Receiver design and analysis over time-varying channels,” *IEEE Open J. Commun. Soc.*, vol. 6, 2025.
- [23] D. Wulich, “Comments on the peak factor of sampled and continuous signals,” *IEEE Wireless Commun. Lett.*, vol. 4, no. 7, Jul. 2000.
- [24] M. Sharif, M. Gharavi-Alkhanisari, and B. Khalaj, “On the peak-to-average power of OFDM signals based on oversampling,” *IEEE Trans. Commun.*, vol. 51, no. 1, pp. 72–78, Jan. 2003.
- [25] M. Mirabella, P. Di Vestì, and G. M. Vitetta, “A Novel Message Passing Algorithm for Soft-Output Detection in Faster-than-Nyquist Multicarrier Systems,” in *2025 IEEE 26th Int. Workshop Signal Process. Artif. Intell. for Wireless Commun. (SPAWC)*, Jul. 2025, pp. 1–5.
- [26] M. Mirabella, P. Di Vestì, C. Masouros, and G. M. Vitetta, “Joint Range and Doppler Estimation Using Spectrally Efficient FDM,” *IEEE Trans. Wireless Commun.*, vol. 25, pp. 11 113–11 127, Feb. 2026.
- [27] M. S. Omar and X. Ma, “Performance Analysis of OCDM for Wireless Communications,” *IEEE Trans. Wireless Commun.*, vol. 20, no. 7, pp. 4032–4043, Feb. 2021.
- [28] A. Bemani, G. Cuzzo, N. Ksairi, and M. Kountouris, “Affine Frequency Division Multiplexing for Next-Generation Wireless Networks,” in *2021 17th Int. Symp. on Wireless Commun. Sys. (ISWCS)*, Oct. 2021, pp. 1–6.
- [29] Z. Sui *et al.*, “MIMO-AFDM Outperforms MIMO-OFDM in the Face of Hardware Impairments,” 2026. *arxiv:2601.00502*
- [30] Z. Sui *et al.*, “Performance Analysis and Optimization of STAR-RIS-Aided Cell-Free Massive MIMO Systems Relying on Imperfect Hardware,” *IEEE Trans. Wireless Commun.*, vol. 24, no. 4, Jan. 2025.
- [31] P. John G. and M. Salehi, *Digital Comm.*, McGraw-Hill., 2008.
- [32] G. Abreu, “Very simple tight bounds on the q-function,” *IEEE Trans. Commun.*, vol. 60, no. 9, pp. 2415–2420, 2012.
- [33] S. M. Kay, *Fundamentals of statistical signal processing: estimation theory*. Prentice-Hall, Inc., 1993.
- [34] 3rd Generation Partnership Project (3GPP), “Study on channel model for frequencies from 0.5 to 100 GHz,” April 2022, Tech. Rep. 38.901 v17.0.0, Available at ETSI.